

Impact of tiny Fermi pockets with extremely high mobility on the Hall anomaly in the kagome metal CsV_3Sb_5

S. Liu^{1,*}, M. Roppongi¹, M. Kimata^{2,3}, K. Ishihara¹, R. Grasset⁴, M. Konczykowski⁴,
B. R. Ortiz⁵, S. D. Wilson⁶, K. Yoshimi⁷, T. Shibauchi^{1,†} and K. Hashimoto^{1,‡}

¹*Department of Advanced Materials Science, University of Tokyo, Kashiwa, Chiba 277-8561, Japan*

²*Institute for Material Research, Tohoku University, Sendai, Miyagi 980-8577 464-8602, Japan*

³*Advanced Science Research Center, Japan Atomic Energy Agency, Tokai, Ibaraki 319-1195, Japan*

⁴*Laboratoire des Solides Irradiés, CEA/DRF/IRAMIS, Ecole Polytechnique, CNRS, Institut Polytechnique de Paris, F-91128 Palaiseau, France*

⁵*Materials Science and Technology Division, Oak Ridge National Laboratory, Oak Ridge, TN 37831, USA*

⁶*Materials Department, University of California Santa Barbara, Santa Barbara, CA 93106, USA*

⁷*Institute of Solid Physics, University of Tokyo, Kashiwa, Chiba 277-8581, Japan*

The kagome metal CsV_3Sb_5 exhibits an unusual charge-density-wave (CDW) order, where the emergence of loop current order that breaks time-reversal symmetry (TRS) has been proposed. A key feature of this CDW phase is a non-monotonic Hall effect at low fields, often attributed to TRS breaking. However, its origin remains unclear. Here, we conduct comprehensive magnetotransport measurements on CsV_3Sb_5 and, through mobility spectrum analysis, identify the formation of tiny Fermi pockets with extremely high mobility below the CDW transition. Furthermore, electron irradiation experiments reveal that the non-monotonic Hall effect is significantly suppressed in samples with reduced mobility, despite no substantial change in the electronic structure. These results indicate that the non-monotonic Hall effect originates from these tiny Fermi pockets with high mobility carriers rather than anomalous Hall mechanisms, providing new insights into understanding the Hall anomaly in this kagome system.

The recently discovered kagome metals $A\text{V}_3\text{Sb}_5$ ($A = \text{K}, \text{Rb}, \text{Cs}$) have garnered considerable attention as a platform for exploring various nontrivial quantum phases predicted in kagome lattice systems [1]. This family features a perfect kagome lattice formed by V atoms, resulting in a unique band structure with Dirac cones and van Hove singularities near the Fermi energy, which are characteristic of ideal kagome lattices [2–4]. Theoretically, these van Hove singularities are expected to induce instabilities that drive unconventional charge-density-wave (CDW) and superconducting states [1, 5, 6]. Indeed, these materials undergo a CDW transition at $T_{\text{CDW}} = 78\text{--}103\text{ K}$ [1, 7, 8], characterized by lattice modulations with star-of-David and/or inverse star-of-David (trihexagonal) patterns [9–12], followed by a superconducting transition at $T_c = 0.9\text{--}2.5\text{ K}$ [1, 8, 13].

In these kagome materials, several exotic phenomena, such as time-reversal symmetry (TRS) and rotational symmetry breakings, have been reported in relation to the CDW order. For instance, various experiments, including muon spin relaxation (μSR) [14, 15], Kerr effect [16, 17], scanning tunneling microscopy (STM) [18–20], and magnetic torque measurements [21], have pointed out the emergence of TRS breaking associated with the CDW order, and its possible connection to loop current order has been discussed [22]. Intriguingly, in this system, a non-monotonic Hall effect has been observed at low fields below T_{CDW} [23–25]. The origin of this non-monotonic Hall effect has been discussed in terms of various anomalous Hall mechanisms, including skew scattering caused by spin clusters [23],

Berry curvature arising from a topological band structure [26, 27], and spontaneous magnetization due to loop current order [18, 21, 28]. In addition to these mechanisms, the band structure associated with van Hove singularities has also been considered as a possible origin of the Hall anomaly [29]. However, despite extensive experimental and theoretical investigations, the origin of the Hall anomaly remains an open question.

Quantum oscillation experiments in this kagome system have shown that the Fermi surfaces are reconstructed at the CDW transition, resulting in the formation of multiple small Fermi surfaces with light effective masses [24, 26, 27, 30–36]. Importantly, multiband systems with small Fermi surfaces hosting high-mobility carriers often exhibit non-monotonic Hall effects at relatively low magnetic fields. However, in this kagome system, a comprehensive analysis of magnetotransport properties that fully incorporates the multiband effect is limited, largely due to the complexity of accounting for multiple Fermi surfaces. In this study, we conduct extensive magnetotransport measurements on CsV_3Sb_5 to clarify the origin of the non-monotonic Hall effect, with careful consideration of the multiband effect. Using mobility spectrum (μ -spectrum) analysis, which does not require assumptions regarding the number or types of carriers [37–40], we demonstrate that the non-monotonic Hall effect originates from small Fermi pockets with high-mobility carriers. Furthermore, we confirm from the investigation of impurity effects that the non-monotonic Hall effect does not originate from anomalous Hall mechanisms.

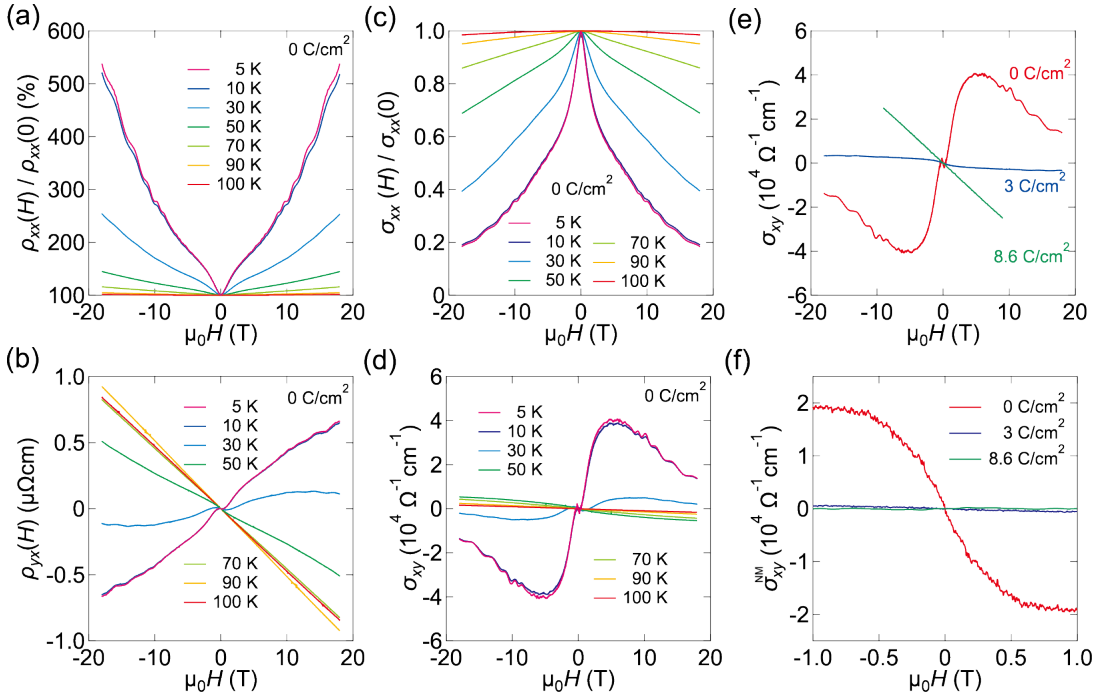


FIG. 1. (a) Normalized MR of pristine CsV_3Sb_5 as a function of magnetic field applied along the c -axis, measured at various temperatures. (b) Hall resistivity of pristine CsV_3Sb_5 as a function of field along the c -axis, measured at various temperatures. (c) Normalized MC of pristine CsV_3Sb_5 , measured at various temperatures. (d) Hall conductivity of pristine CsV_3Sb_5 as a function of field, measured at various temperatures. (e) Hall conductivity of pristine and electron-irradiated CsV_3Sb_5 samples as a function of field, measured at 5 K. (f) Hall conductivity with the ordinary Hall component (proportional to the field) subtracted at 5 K for pristine and irradiated CsV_3Sb_5 samples as a function of field.

High-quality single crystals of CsV_3Sb_5 were synthesized using the self-flux growth method [1]. Magnetotransport measurements were conducted via a conventional five-probe method, using an 18-T superconducting magnet at the Institute for Materials Research, Tohoku University, and a Physical Property Measurement System (PPMS) up to 9 T from Quantum Design. Electron irradiation at an incident energy of 2.5 MeV was carried out at the SIRIUS Pelletron accelerator, operated by the Laboratoire des Solides irradiés (LSI) at École Polytechnique. The μ -spectrum analysis was performed using the Gpufit package in Python [41], and final fitting confirmation was conducted within the 2DMAT framework [42].

Figure 1(a) shows the field dependence of the magnetoresistivity (MR) normalized by its zero-field value, $\rho_{xx}(H)/\rho_{xx}(0)$, measured up to ± 18 T at various temperatures for the pristine CsV_3Sb_5 sample. As the temperature decreases, the MR increases rapidly, and Shubnikov-de Hass (SdH) quantum oscillations become pronounced. Figure 1(b) presents the Hall resistivity $\rho_{yx}(H)$ as a function of field up to ± 18 T for the pristine sample. At 100 K, ρ_{yx} is negative, but as the temperature decreases, its slope gradually decreases and eventually turns positive below ~ 30 K. Additionally, a non-monotonic Hall effect is observed in the low-field region below ~ 1 T. These results are consistent with previous studies [24, 30]. Fig-

ures 1(c) and 1(d) show the field dependence of the normalized magnetoconductivity (MC), $\sigma_{xx}(H)/\sigma_{xx}(0)$, and the Hall conductivity, $\sigma_{xy}(H)$, for the pristine sample, respectively. The Hall anomaly in the low-field region is clearly visible at low temperatures.

First, we analyze the SdH quantum oscillations. Generally, the MR is fitted with a quadratic function to extract the oscillatory components. However, as shown in Fig. 1(a), the MR of CsV_3Sb_5 exhibits a non-quadratic dependence in the low-field region around 1–2 T, preventing a straightforward fit across the entire field range. Then, to obtain the non-oscillatory component of ρ_{xx}^{bg} , we simultaneously fit $\sigma_{xx}(H)$ and $\sigma_{xy}(H)$ using generalized Lorentzian functions based on the μ -spectrum analysis (see Supplemental Material). As a result, we obtain the non-oscillatory components of σ_{xx}^{bg} and σ_{xy}^{bg} , yielding $\rho_{xx}^{\text{bg}} = \sigma_{xx}^{\text{bg}} / [(\sigma_{xx}^{\text{bg}})^2 + (\sigma_{xy}^{\text{bg}})^2]$. Figure 2(a) shows the oscillatory components $\Delta\rho(H) = \rho_{xx}(H) - \rho_{xx}^{\text{bg}}(H)$ at various temperatures. Clear quantum oscillations are observed below 50 K. Figure 2(b) displays the fast Fourier transform (FFT) of the oscillatory components in Fig. 2(a), revealing four distinct frequencies at 18 T, 25 T, 73 T, and 92 T, labeled as α, β, γ , and δ , respectively. Each frequency F corresponds to the extremal cross-sectional area A_F of each Fermi surface, as expressed by the Onsager relation $F = (\hbar/2\pi e)A_F$. The

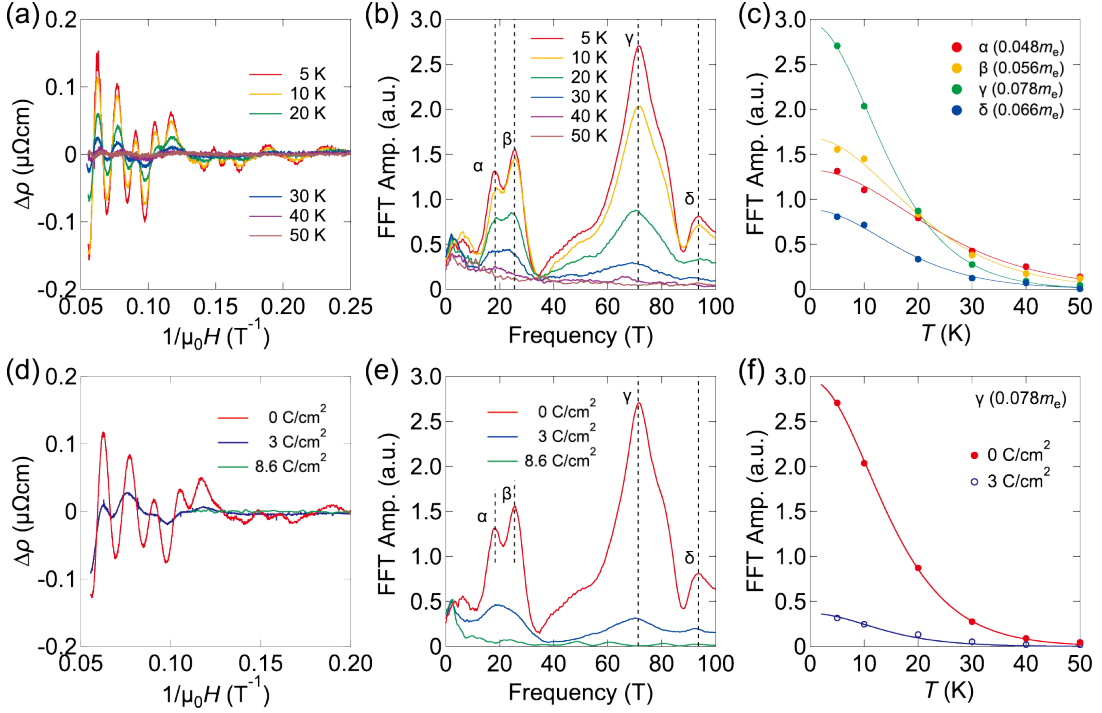


FIG. 2. (a) Oscillatory components extracted from the MR of the pristine sample at various temperatures. (b) FFT spectrum of the pristine sample at various temperatures. (c) Temperature dependence of the FFT amplitude for each orbit. The solid lines represent the fits to the Lifshitz-Kosevich formula. Here, m_e is the free electron mass. (d) Oscillatory components extracted from the MR of the pristine and irradiated samples measured at 5 K. (e) FFT spectrum of the pristine and irradiated samples at 5 K. (f) FFT amplitudes of the γ orbit for the pristine and 3 C/cm² irradiated samples. For both samples, the effective mass obtained using the LK formula is $m_{\text{eff}} = 0.078m_e$.

A_F values obtained for these frequencies are equivalent to $0.0044A_{\text{BZ}}$, $0.0062A_{\text{BZ}}$, $0.018A_{\text{BZ}}$, and $0.023A_{\text{BZ}}$, where A_{BZ} is the area of the Brillouin zone (BZ) in the CDW phase, indicating the presence of extremely tiny Fermi pockets. Figure 2(c) presents the temperature dependence of the FFT amplitude for each Fermi pocket, from which the effective cyclotron mass can be evaluated using the Lifshitz-Kosevich (LK) formula, $a_i = (\lambda m_{\text{eff}} T / \mu_0 H_{\text{avg}}) / \sinh(\lambda m_{\text{eff}} T / \mu_0 H_{\text{avg}})$, where a_i is the FFT amplitude, $\lambda = 14.69$ T/K, m_{eff} is the effective cyclotron mass, μ_0 is the vacuum permeability, and H_{avg} is the average value of the magnetic field window used for the FFT. All effective masses obtained here are extremely low, consistent with previous studies [24, 30].

Next, we investigate the effects of these small Fermi pockets on the magnetotransport properties of CsV₃Sb₅. To this end, we employ the μ -spectrum method [37–40], which allows for the analysis of magnetotransport properties without assumptions regarding the number or types of carriers (see Supplemental Material). For this analysis, we first define the normalized MC, $X(H) \equiv \sigma_{xx}(H) / \sigma_{xx}(0)$, and Hall conductivity, $Y(H) \equiv \sigma_{xy}(H) / \sigma_{xx}(0)$, as shown in Figs. 3(a) and 3(b). Generally, the MC and Hall conductivity can be separated into hole and electron contributions, i.e., $X(H) =$

$X^p(H) + X^n(H)$ and $Y(H) = Y^p(H) + Y^n(H)$, where the superscripts p and n represent the contributions from hole and electron carriers, respectively. Additionally, the Kramers-Kronig (KK) relations lead to $X'(H) = Y^p(H) - Y^n(H)$ and $Y'(H) = -X^p(H) + X^n(H)$, where $X'(H)$ and $Y'(H)$ denote the KK transformations of $X(H)$ and $Y(H)$, respectively [37] (see Supplemental Material). Using these relations, we can obtain $X^{p,n}(H)$ and $Y^{p,n}(H)$, as shown in Figs. 3(a) and 3(b).

Here, each component of $X^{p,n}$ and $Y^{p,n}$ can be represented as an integral of Lorentzian functions with respect to the carrier mobility μ as follows [43]:

$$X^{p,n}(H) = \int_0^\infty \frac{s^{p,n}(\mu) d\mu}{1 + \mu^2 B^2}, \quad (1)$$

$$Y^{p,n}(H) = \int_0^\infty \frac{s^{p,n}(\mu) \mu B d\mu}{1 + \mu^2 B^2}, \quad (2)$$

where $s^{p,n}(\mu)$ denotes the normalized conductivity as a function of μ , and $B = \mu_0 H$ represents the magnetic flux density. In this study, to obtain $s^{p,n}(\mu)$ as a function of μ , we divide μ into N segments so that $\ln(\mu)$ is equally spaced. We then fit $X_{p,n}(H)$ and $Y_{p,n}(H)$ for N different magnetic fields, using $s^{p,n}(\mu_j)$ as a fitting parameter for each μ_j ($j = 1 \sim N$) (see Supplemental Material).

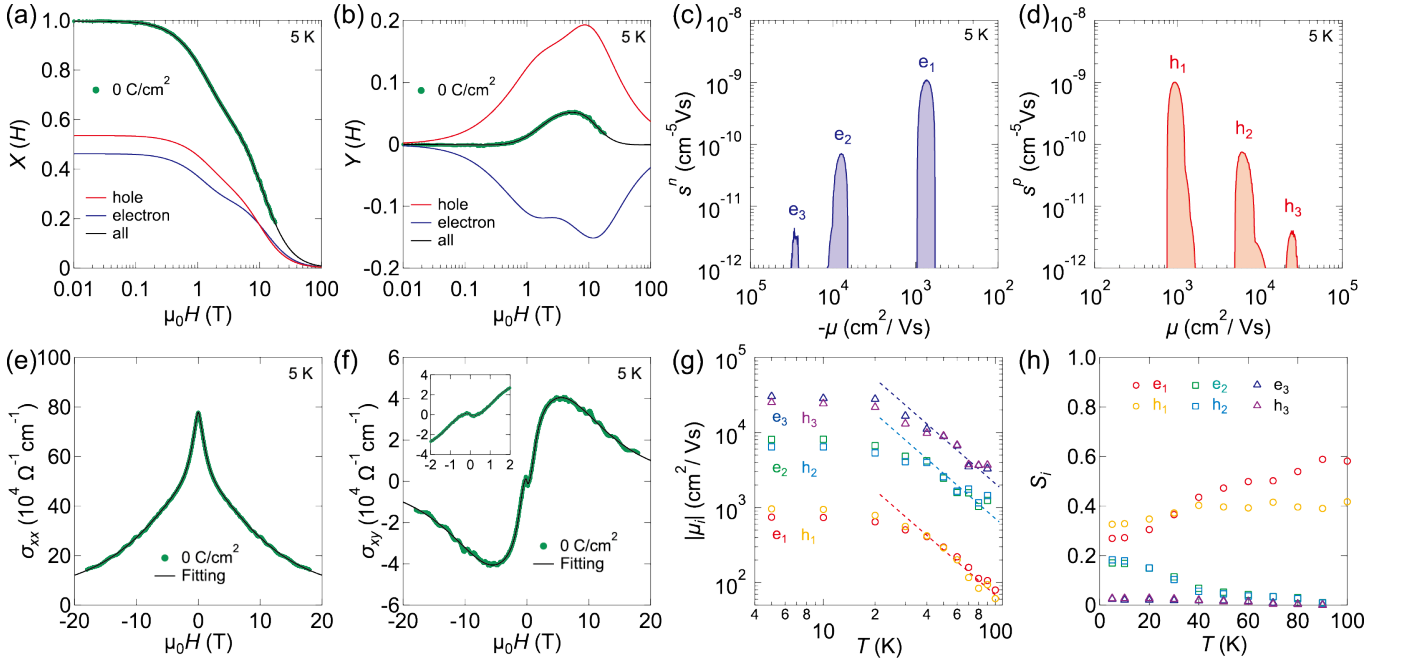


FIG. 3. (a), (b) Normalized MC, $X(H)$, and Hall conductivity, $Y(H)$, calculated at 5 K for pristine CsV_3Sb_5 , respectively. The black lines represent Lorentzian fits to the experimental results (green). Red and blue lines indicate contributions from hole and electron carriers, respectively. (c), (d) Normalized conductivity spectra as a function of mobility for hole and electron carriers in pristine CsV_3Sb_5 at 5 K, respectively. (e), (f) Comparisons between experimental and fitting results for $\sigma_{xx}(H)$ and $\sigma_{xy}(H)$, respectively. The inset in (f) shows the expanded view in the low-field region. (g), (h) Temperature dependence of the averaged mobility $|\mu_i|$ of each carrier and the contribution of each carrier to the total conductivity S_i . The dashed lines in (g) indicate a T^{-2} dependence.

Figures 3(c) and 3(d) show the normalized conductivity spectrum obtained at 5 K, where positive (negative) mobility corresponds to hole (electron) carriers. The s^p, n^p spectrum reveals three distinct peaks for both hole and electron carriers, indicating the presence of three hole carriers (h_1, h_2 , and h_3) and three electron carriers (e_1, e_2 , and e_3). Subsequently, we calculated the averaged mobility (μ_i) and the contribution of each peak i ($= e_1 - e_3, h_1 - h_3$) to the total conductivity (S_i). Using these values as initial parameters, we fitted $\sigma_{xx}(H)$ and $\sigma_{xy}(H)$ with Lorentzian functions (see Supplemental Material). As a result, as shown in Figs. 3(e) and 3(f), the fitted MC and Hall conductivity exhibit good agreement with the experimental results.

Figure 3(g) shows the temperature dependence of the mobility $|\mu_i|$ of each carrier in the CDW phase of pristine CsV_3Sb_5 . At high temperatures, the mobility of all carriers follows typical Fermi liquid behavior ($\propto 1/T^2$) but saturates below 30 K due to impurity scatterings. Notably, the four carriers, h_2, h_3, e_2 , and e_3 , exhibit extremely high mobility ($\gtrsim \sim 10,000 \text{ cm}^2/\text{Vs}$) at low temperatures. Given their extremely low effective masses, these carriers may originate from Dirac dispersions. The comparison between the μ -spectrum analysis and the quantum oscillation results suggests that the h_2, h_3, e_2 , and e_3 carriers correspond to the α - δ orbits, whereas the h_1 and

e_1 carriers are assigned to larger Fermi surfaces around the Γ and K points in the original BZ (see Supplemental Material). Figure 3(h) shows the temperature dependence of the contribution of each carrier to the total conductivity S_i . Although the mobilities of h_1 and e_1 are not particularly high ($\sim 1,000 \text{ cm}^2/\text{Vs}$), their carrier densities are much larger than those of the other four carriers, suggesting that the sign of the Hall effect is determined by the balance between h_1 and e_1 . Indeed, the contributions from h_1 and e_1 to the total conductivity are reversed at 30 K, where the sign of the Hall effect is also reversed (see Fig. 1(b)). On the other hand, the remaining four carriers, h_2, h_3, e_2 , and e_3 , are characterized by extremely high mobility and low-carrier density, which are expected to play a dominant role in the magnetotransport properties at low temperatures and low magnetic fields.

To examine whether the non-monotonic Hall effect originates from the small Fermi pockets with high-mobility carriers, we investigated the impurity effect on magnetotransport properties of CsV_3Sb_5 , using the electron irradiation technique. It is well known that electron irradiation can create non-magnetic point defects without changing the lattice constants and carrier concentration of the sample [44, 45]. To verify that the electronic structure remains unaffected by electron irradiation, we analyzed the SdH quantum oscillations. Figure 2(d) il-

illustrates the SdH oscillatory components for the samples with irradiated doses of 0 (pristine), 3, and 8.6 C/cm². The oscillation period is unaffected by electron irradiation, as confirmed by the FFT results of the oscillatory components (see Fig. 2(e)). The effective mass of the γ orbit for the pristine and 3 C/cm² irradiated samples remains unchanged by electron irradiation (see Fig. 2(f)). These results indicate that the Fermi surface structure is essentially unchanged by electron irradiation, and that electron irradiation primarily causes a reduction in the mean free path of the carriers.

Figure 1(e) presents the field dependence of the Hall conductivity for irradiation doses of 0, 3, and 8.6 C/cm² measured at 5 K. With increasing irradiation dose, the non-monotonic behavior of the Hall effect in the low-field region is largely suppressed, accompanied by a shift of the dominant carrier contribution from hole to electron. The Hall anomaly observed at low fields in this kagome system is often attributed to anomalous Hall mechanisms. Generally, the anomalous Hall effect arising from Berry curvature is dominated by the topological band structure and should be robust against impurities. However, we find that although electron irradiation only changes the mobility without affecting the band structure, the non-monotonic Hall component below ~ 1 T is significantly suppressed by electron irradiation (see Fig. 1(f)). This fact strongly suggests that the non-monotonic Hall effect at low fields originates not from Berry curvature, but rather from the small Fermi pockets with high mobility.

In the case of the anomalous Hall effect arising from loop current order, σ_{xy} becomes independent of σ_{xx} in the moderated scattering regime [22]. However, our results show that $\sigma_{xy} \propto \sigma_{xx}^2$ (see Supplemental Material), which is the typical relationship characteristic of the ordinary Hall effect. Thus, the Hall effect in the present kagome system appears to be governed by the ordinary Hall effect. It is worth noting, however, that our experiments do not rule out the presence of Berry curvature due to loop current order. Generally, the anomalous Hall effect arising from Berry curvature tends to be limited to values around $\sigma_{xy} \sim 1,000 \Omega^{-1} \text{cm}^{-1}$ (see Supplemental Material). In contrast, in this kagome system, σ_{xy} exhibits a significantly larger value around $10,000 \Omega^{-1} \text{cm}^{-1}$ due to the small Fermi pockets with extremely high mobility. Thus, even if the anomalous Hall effect arising from loop current order is present, it should be masked. Further investigations are required to fully understand the loop current order in this system.

In summary, we performed comprehensive magneto-transport measurements on CsV₃Sb₅, uncovering the presence of tiny Fermi pockets with extremely high-mobility carriers below the CDW transition. Furthermore, electron irradiation experiments reveal that the non-monotonic Hall effect is significantly suppressed in samples with reduced mobility, despite the absence of substantial changes to the electronic structure. These

findings indicate that the non-monotonic Hall effect arises from the tiny Fermi pockets with high mobility rather than the anomalous Hall mechanisms.

ACKNOWLEDGMENTS

We thank H. Kontani for fruitful discussions. This work was supported by Grants-in-Aid for Scientific Research (KAKENHI) (Nos. JP24K17007, JP24H01646, JP23H00089, JP22H00105, JP22H01176, JP22H04933, JP22H00109), Grant-in-Aid for Scientific Research on innovative areas ‘‘Quantum Liquid Crystals’’ (No. JP19H05824), Grant-in-Aid for Scientific Research for Transformative Research Areas (A) ‘‘Condensed Conjugation’’ (Nos. JP20H05869, JP21H05470) from Japan Society for the Promotion of Science (JSPS), and JST, PRESTO (No. JPMJPR2458), Japan. This work was performed under the GIMRT Program of the Institute for Materials Research, Tohoku University (Proposal Nos. 202012-HMKPA-0057, 202112-HMKPA-0018, 202212-HMKPA-0055). Electron irradiation experiments performed at the SIRIUS beamline were supported by the EMIR&A French network (FR CNRS 3618). Work by B.R.O. is supported by the U.S. Department of Energy, Office of Science, Basic Energy Sciences, Materials Sciences and Engineering Division. B.R.O. and S.D.W. gratefully acknowledge support via the UC Santa Barbara NSF Quantum Foundry funded via the Q-AMASE-i program under award No. DMR-1906325.

* s.liu@qpm.k.u-tokyo.ac.jp

† shibauchi@k.u-tokyo.ac.jp

‡ k.hashimoto@edu.k.u-tokyo.ac.jp

- [1] B. R. Ortiz, S. M. L. Teicher, Y. Hu, J. L. Zuo, P. M. Sarte, E. C. Schueller, A. M. M. Abeykoon, M. J. Krogstad, S. Rosenkranz, R. Osborn, R. Seshadri, L. Balents, J. He, and S. D. Wilson, CsV₃Sb₅: A Z₂ topological kagome metal with a superconducting ground state, *Phys. Rev. Lett.* **125**, 247002 (2020).
- [2] H. Tan, Y. Liu, Z. Wang, and B. Yan, Charge Density Waves and Electronic Properties of Superconducting Kagome Metals, *Phys. Rev. Lett.* **127**, 046401 (2021).
- [3] M. Kang, S. Fang, J.-K. Kim, B. R. Ortiz, S. H. Ryu, J. Kim, J. Yoo, G. Sangiovanni, D. Di Sante, B.-G. Park, C. Jozwiak, A. Bostwick, E. Rotenberg, E. Kaxiras, S. D. Wilson, J.-H. Park, and R. Comin, Twofold van Hove singularity and origin of charge order in topological kagome superconductor CsV₃Sb₅, *Nature Physics* **18**, 301 (2022).
- [4] Y. Hu, X. Wu, B. R. Ortiz, S. Ju, X. Han, J. Ma, N. C. Plumb, M. Radovic, R. Thomale, S. D. Wilson, A. P. Schnyder, and M. Shi, Rich nature of Van Hove singularities in Kagome superconductor CsV₃Sb₅, *Nature Communications* **13**, 2220 (2022).
- [5] Y.-P. Lin and R. M. Nandkishore, Complex charge density waves at Van Hove singularity on hexagonal lattices:

- Haldane-model phase diagram and potential realization in the kagome metals AV_3Sb_5 (AV_3Sb_5 ($A = K, Rb, Cs$)), *Phys. Rev. B* **104**, 045122 (2021).
- [6] X. Wu, T. Schwemmer, T. Müller, A. Consiglio, G. Sangiovanni, D. Di Sante, Y. Iqbal, W. Hanke, A. P. Schnyder, M. M. Denner, M. H. Fischer, T. Neupert, and R. Thomale, Nature of unconventional pairing in the kagome superconductors AV_3Sb_5 ($A = K, Rb, Cs$), *Phys. Rev. Lett.* **127**, 177001 (2021).
- [7] B. R. Ortiz, L. C. Gomes, J. R. Morey, M. Winiarski, M. Bordelon, J. S. Mangum, I. W. H. Oswald, J. A. Rodriguez-Rivera, J. R. Neilson, S. D. Wilson, E. Ertekin, T. M. McQueen, and E. S. Toberer, New kagome prototype materials: discovery of KV_3Sb_5 , RbV_3Sb_5 , and CsV_3Sb_5 , *Phys. Rev. Mater.* **3**, 094407 (2019).
- [8] B. R. Ortiz, P. M. Sarte, E. M. Kenney, M. J. Graf, S. M. L. Teicher, R. Seshadri, and S. D. Wilson, Superconductivity in the \mathbb{Z}_2 kagome metal KV_3Sb_5 , *Phys. Rev. Mater.* **5**, 034801 (2021).
- [9] L. Kautzsch, B. R. Ortiz, K. Mallayya, J. Plumb, G. Pokharel, J. P. C. Ruff, Z. Islam, E.-A. Kim, R. Seshadri, and S. D. Wilson, Structural evolution of the kagome superconductors AV_3Sb_5 ($A = K, Rb, Cs$) through charge density wave order, *Phys. Rev. Mater.* **7**, 024806 (2023).
- [10] J. Frassinetti, P. Bonfà, G. Allodi, E. Garcia, R. Cong, B. R. Ortiz, S. D. Wilson, R. De Renzi, V. F. Mitrović, and S. Sanna, Microscopic nature of the charge-density wave in the kagome superconductor RbV_3Sb_5 , *Phys. Rev. Res.* **5**, L012017 (2023).
- [11] Q. Stahl, D. Chen, T. Ritschel, C. Shekhar, E. Sadrollahi, M. C. Rahn, O. Ivashko, M. v. Zimmermann, C. Felser, and J. Geck, Temperature-driven reorganization of electronic order in CsV_3Sb_5 , *Phys. Rev. B* **105**, 195136 (2022).
- [12] Q. Xiao, Y. Lin, Q. Li, X. Zheng, S. Francoual, C. Plueckthun, W. Xia, Q. Qiu, S. Zhang, Y. Guo, J. Feng, and Y. Peng, Coexistence of multiple stacking charge density waves in kagome superconductor CsV_3Sb_5 , *Phys. Rev. Res.* **5**, L012032 (2023).
- [13] Q. Yin, Z. Tu, C. Gong, Y. Fu, S. Yan, and H. Lei, Superconductivity and normal-state properties of kagome metal RbV_3Sb_5 single crystals, *Chinese Physics Letters* **38**, 037403 (2021).
- [14] C. Mielke, D. Das, J.-X. Yin, H. Liu, R. Gupta, Y.-X. Jiang, M. Medarde, X. Wu, H. C. Lei, J. Chang, P. Dai, Q. Si, H. Miao, R. Thomale, T. Neupert, Y. Shi, R. Khasanov, M. Z. Hasan, H. Luetkens, and Z. Guguchia, Time-reversal symmetry-breaking charge order in a kagome superconductor, *Nature* **602**, 245 (2022).
- [15] L. Yu, C. Wang, Y. Zhang, M. Sander, S. Ni, Z. Lu, S. Ma, Z. Wang, Z. Zhao, H. Chen, K. Jiang, Y. Zhang, H. Yang, F. Zhou, X. Dong, S. L. Johnson, M. J. Graf, J. Hu, H.-J. Gao, and Z. Zhao, Evidence of a hidden flux phase in the topological kagome metal CsV_3Sb_5 (2021), [arXiv:2107.10714 \[cond-mat.supr-con\]](https://arxiv.org/abs/2107.10714).
- [16] D. R. Saykin, C. Farhang, E. D. Kountz, D. Chen, B. R. Ortiz, C. Shekhar, C. Felser, S. D. Wilson, R. Thomale, J. Xia, and A. Kapitulnik, High resolution polar Kerr effect studies of CsV_3Sb_5 : Tests for time-reversal symmetry breaking below the charge-order transition, *Phys. Rev. Lett.* **131**, 016901 (2023).
- [17] Y. Hu, S. Yamane, G. Mattoni, K. Yada, K. Obata, Y. Li, Y. Yao, Z. Wang, J. Wang, C. Farhang, J. Xia, Y. Maeno, and S. Yonezawa, Time-reversal symmetry breaking in charge density wave of CsV_3Sb_5 detected by polar Kerr effect (2023), [arXiv:2208.08036 \[cond-mat.str-el\]](https://arxiv.org/abs/2208.08036).
- [18] Y.-X. Jiang, J.-X. Yin, M. M. Denner, N. Shumiya, B. R. Ortiz, G. Xu, Z. Guguchia, J. He, M. S. Hossain, X. Liu, J. Ruff, L. Kautzsch, S. S. Zhang, G. Chang, I. Belopolski, Z.-J. Cheng, X. P. Yang, Z. Wang, R. Thomale, T. Neupert, S. D. Wilson, and M. Z. Hasan, Unconventional chiral charge order in kagome superconductor KV_3Sb_5 , *Nature Materials* **20**, 1353 (2021).
- [19] H. Zhao, H. Li, B. R. Ortiz, S. M. L. Teicher, T. Park, M. Ye, Z. Wang, L. Balents, S. D. Wilson, and I. Zeljkovic, Cascade of correlated electron states in the kagome superconductor CsV_3Sb_5 , *Nature* **599**, 216 (2021).
- [20] Z. Wang, Y.-X. Jiang, J.-X. Yin, Y. Li, G.-Y. Wang, H.-L. Huang, S. Shao, J. Liu, P. Zhu, N. Shumiya, M. S. Hossain, H. Liu, Y. Shi, J. Duan, X. Li, G. Chang, P. Dai, Z. Ye, G. Xu, Y. Wang, H. Zheng, J. Jia, M. Z. Hasan, and Y. Yao, Electronic nature of chiral charge order in the kagome superconductor CsV_3Sb_5 , *Phys. Rev. B* **104**, 075148 (2021).
- [21] T. Asaba, A. Onishi, Y. Kageyama, T. Kiyosue, K. Ohtsuka, S. Suetsugu, Y. Kohsaka, T. Gaggli, Y. Kasahara, H. Murayama, K. Hashimoto, R. Tazai, H. Kontani, B. R. Ortiz, S. D. Wilson, Q. Li, H.-H. Wen, T. Shibauchi, and Y. Matsuda, Evidence for an odd-parity nematic phase above the charge-density-wave transition in a kagome metal, *Nature Physics* **20**, 40 (2024).
- [22] R. Tazai, Y. Yamakawa, and H. Kontani, Charge-loop current order and \mathbb{Z}_3 nematicity mediated by bond order fluctuations in kagome metals, *Nature Communications* **14**, 7845 (2023).
- [23] S.-Y. Yang, Y. Wang, B. R. Ortiz, D. Liu, J. Gayles, E. Derunova, R. Gonzalez-Hernandez, L. Šmejkal, Y. Chen, S. S. P. Parkin, S. D. Wilson, E. S. Toberer, T. McQueen, and M. N. Ali, Giant, unconventional anomalous Hall effect in the metallic frustrated magnet candidate, KV_3Sb_5 , *Science Advances* **6**, eabb6003 (2020).
- [24] F. H. Yu, T. Wu, Z. Y. Wang, B. Lei, W. Z. Zhuo, J. J. Ying, and X. H. Chen, Concurrence of anomalous Hall effect and charge density wave in a superconducting topological kagome metal, *Phys. Rev. B* **104**, L041103 (2021).
- [25] L. Wang, W. Zhang, Z. Wang, T. F. Poon, W. Wang, C. W. Tsang, J. Xie, X. Zhou, Y. Zhao, S. Wang, K. T. Lai, and S. K. Goh, Anomalous Hall effect and two-dimensional Fermi surfaces in the charge-density-wave state of kagome metal RbV_3Sb_5 , *Journal of Physics: Materials* **6**, 02LT01 (2023).
- [26] Y. Fu, N. Zhao, Z. Chen, Q. Yin, Z. Tu, C. Gong, C. Xi, X. Zhu, Y. Sun, K. Liu, and H. Lei, Quantum transport evidence of topological band structures of kagome superconductor CsV_3Sb_5 , *Phys. Rev. Lett.* **127**, 207002 (2021).
- [27] R. Chapai, M. Leroux, V. Oliviero, D. Vignolles, N. Bruyant, M. P. Smylie, D. Y. Chung, M. G. Kanatzidis, W.-K. Kwok, J. F. Mitchell, and U. Welp, Magnetic breakdown and topology in the kagome superconductor CsV_3Sb_5 under high magnetic field, *Phys. Rev. Lett.* **130**, 126401 (2023).

- [28] C. Guo, C. Putzke, S. Konyzheva, X. Huang, M. Gutierrez-Amigo, I. Errea, D. Chen, M. G. Vergniory, C. Felser, M. H. Fischer, T. Neupert, and P. J. W. Moll, Switchable chiral transport in charge-ordered kagome metal CsV_3Sb_5 , *Nature* **611**, 461 (2022).
- [29] A. E. Koshelev, R. Chapai, D. Y. Chung, J. F. Mitchell, and U. Welp, Origin of anomalous magnetotransport in kagome superconductors av_3sb_5 ($a = \text{K,rb,cs}$), *Phys. Rev. B* **110**, 024512 (2024).
- [30] B. R. Ortiz, S. M. L. Teicher, L. Kautzsch, P. M. Sarte, N. Ratcliff, J. Harter, J. P. C. Ruff, R. Seshadri, and S. D. Wilson, Fermi surface mapping and the nature of charge-density-wave order in the kagome superconductor CsV_3Sb_5 , *Phys. Rev. X* **11**, 041030 (2021).
- [31] C. Broyles, D. Graf, H. Yang, X. Dong, H. Gao, and S. Ran, Effect of the interlayer ordering on the Fermi surface of kagome superconductor CsV_3Sb_5 by quantum oscillations, *Phys. Rev. Lett.* **129**, 157001 (2022).
- [32] H. Tan, Y. Li, Y. Liu, D. Kaplan, Z. Wang, and B. Yan, Emergent topological quantum orbits in the charge density wave phase of kagome metal CsV_3Sb_5 , *npj Quantum Materials* **8**, 39 (2023).
- [33] Y. Gan, W. Xia, L. Zhang, K. Yang, X. Mi, A. Wang, Y. Chai, Y. Guo, X. Zhou, and M. He, Magneto-Seebeck effect and ambipolar Nernst effect in the CsV_3Sb_5 superconductor, *Phys. Rev. B* **104**, L180508 (2021).
- [34] D. Chen, B. He, M. Yao, Y. Pan, H. Lin, W. Schnelle, Y. Sun, J. Gooth, L. Taillefer, and C. Felser, Anomalous thermoelectric effects and quantum oscillations in the kagome metal CsV_3Sb_5 , *Phys. Rev. B* **105**, L201109 (2022).
- [35] W. Zhang, L. Wang, C. W. Tsang, X. Liu, J. Xie, W. C. Yu, K. T. Lai, and S. K. Goh, Emergence of large quantum oscillation frequencies in thin flakes of the kagome superconductor CsV_3Sb_5 , *Phys. Rev. B* **106**, 195103 (2022).
- [36] K. Shrestha, R. Chapai, B. K. Pokharel, D. Miertschin, T. Nguyen, X. Zhou, D. Y. Chung, M. G. Kanatzidis, J. F. Mitchell, U. Welp, D. Popović, D. E. Graf, B. Lorenz, and W. K. Kwok, Nontrivial Fermi surface topology of the kagome superconductor CsV_3Sb_5 probed by de Haas-van Alphen oscillations, *Phys. Rev. B* **105**, 024508 (2022).
- [37] J. W. McClure, Analysis of multicarrier galvanomagnetic data for graphite, *Phys. Rev.* **112**, 715 (1958).
- [38] W. A. Beck and J. R. Anderson, Determination of electrical transport properties using a novel magnetic field dependent Hall technique, *Journal of Applied Physics* **62**, 541 (1987).
- [39] J. Antoszewski, G. A. Umana-Membreno, and L. Faraone, High-resolution mobility spectrum analysis of multicarrier transport in advanced infrared materials, *Journal of Electronic Materials* **41**, 2816 (2012).
- [40] K. K. Huynh, Y. Tanabe, T. Urata, S. Heguri, K. Tanigaki, T. Kida, and M. Hagiwara, Mobility spectrum analytical approach for intrinsic band picture of $\text{Ba}(\text{FeAs})_2$, *New Journal of Physics* **16**, 093062 (2014).
- [41] A. Przybylski, B. Thiel, J. Keller-Findeisen, B. Stock, and M. Bates, Gpufit: An open-source toolkit for GPU-accelerated curve fitting, *Scientific Reports* **7**, 15722 (2017).
- [42] Y. Motoyama, K. Yoshimi, I. Mochizuki, H. Iwamoto, H. Ichinose, and T. Hoshi, Data-analysis software framework 2DMAT and its application to experimental measurements for two-dimensional material structures, *Computer Physics Communications* **280**, 108465 (2022).
- [43] J. W. McClure, Field dependence of magnetoconductivity, *Phys. Rev.* **101**, 1642 (1956).
- [44] Y. Mizukami, M. Konczykowski, Y. Kawamoto, S. Kurata, S. Kasahara, K. Hashimoto, V. Mishra, A. Kreisler, Y. Wang, P. J. Hirschfeld, Y. Matsuda, and T. Shibauchi, Disorder-induced topological change of the superconducting gap structure in iron pnictides, *Nature Communications* **5**, 5657 (2014).
- [45] M. Roppongi, K. Ishihara, Y. Tanaka, K. Ogawa, K. Okada, S. Liu, K. Mukasa, Y. Mizukami, Y. Uwatoko, R. Grasset, M. Konczykowski, B. R. Ortiz, S. D. Wilson, K. Hashimoto, and T. Shibauchi, Bulk evidence of anisotropic s -wave pairing with no sign change in the kagome superconductor CsV_3Sb_5 , *Nature Communications* **14**, 667 (2023).

Supplemental Material for

Impact of tiny Fermi pockets with extremely high mobility on the Hall anomaly in the kagome metal CsV_3Sb_5

S. Liu*, M. Roppongi, M. Kimata, K. Ishihara, R. Grasset, M. Konczykowski, B. R. Ortiz,
S. D. Wilson, K. Yoshimi, T. Shibauchi[†], and K. Hashimoto[‡]

* s.liu@qpm.k.u-tokyo.ac.jp

[†] shibauchi@k.u-tokyo.ac.jp

[‡] k.hashimoto@edu.k.u-tokyo.ac.jp

This PDF file includes:

Supplementary Text

Figures S1 to S6

Table S1

Supplementary References

I. MANGETOTRANSPORT MEASUREMENTS

We measured the raw data $\rho_{xx}^{\text{raw}}(H)$ and $\rho_{yx}^{\text{raw}}(H)$ in both positive and negative magnetic fields and symmetrized the data using the following formula:

$$\rho_{xx}(H) = \frac{1}{2}(\rho_{xx}^{\text{raw}}(H) + \rho_{xx}^{\text{raw}}(-H)), \quad (\text{S1})$$

$$\rho_{yx}(H) = \frac{1}{2}(\rho_{yx}^{\text{raw}}(H) - \rho_{yx}^{\text{raw}}(-H)). \quad (\text{S2})$$

Figure S1 presents $\rho_{xx}(H)/\rho_{xx}(0)$ and $\rho_{yx}(H)$ as a function of magnetic field for pristine (0 C/cm^2), 3 C/cm^2 , and 8.6 C/cm^2 electron-irradiated CsV_3Sb_5 samples. As the irradiation dose increases, the increase in magnetoresistance against magnetic fields is significantly suppressed, and the pronounced temperature dependence of the Hall resistivity becomes negligibly small.

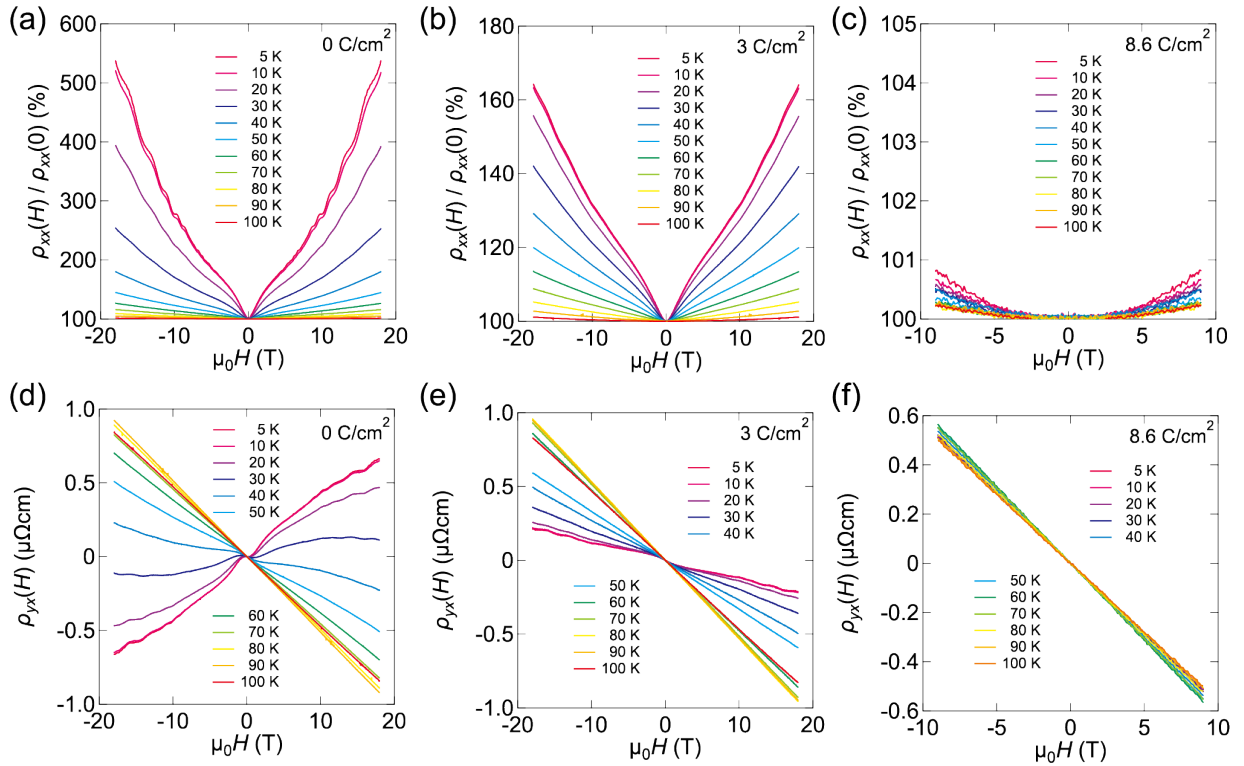


FIG. S1. (a)-(c) Normalized magnetoresistance $\rho_{xx}(H)/\rho_{xx}(0)$ of (a) pristine (0 C/cm^2), (b) 3 C/cm^2 , and (c) 8.6 C/cm^2 irradiated CsV_3Sb_5 samples as a function of magnetic field measured at several temperatures. (d)-(f) Hall resistance $\rho_{yx}(H)$ of (d) pristine (0 C/cm^2), (e) 3 C/cm^2 , and (f) 8.6 C/cm^2 irradiated CsV_3Sb_5 samples as a function of magnetic field measured at several temperatures.

II. μ -SPECTRUM ANALYSIS

In this study, we employed the μ -spectrum method [S1–S4] to extract the conductivity spectrum as a function of mobility μ from magnetotransport measurements. The detailed analysis process is illustrated in Fig. S2 and is described in the following subsections.

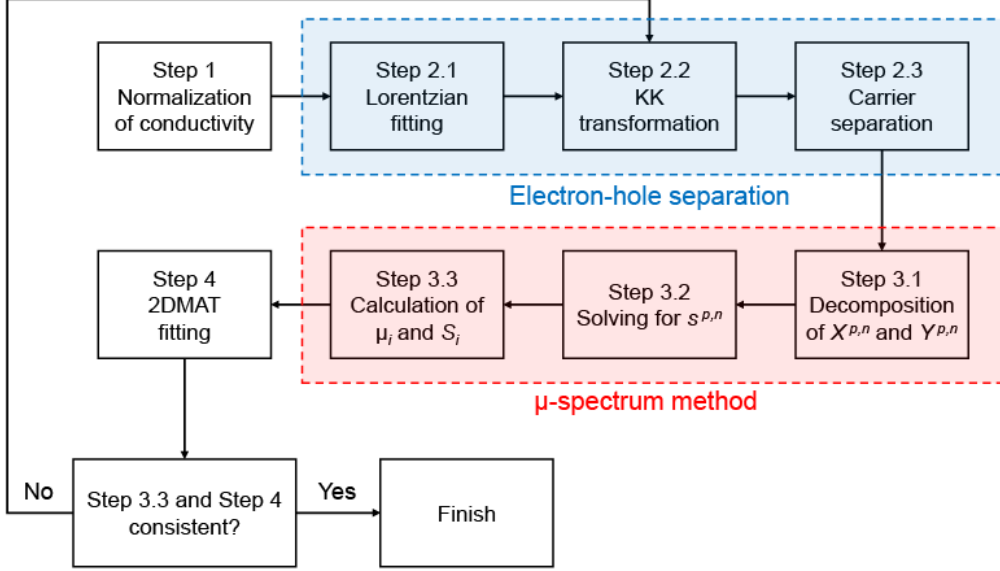


FIG. S2. Overview of the analysis process using the μ -spectrum method.

1. Normalization of conductivity

The first step is to derive the magnetoconductivity $\sigma_{xx}(H)$ and Hall conductivity $\sigma_{xy}(H)$ from the measured magnetoresistivity $\rho_{xx}(H)$ and Hall resistivity $\rho_{yx}(H)$ using the following relations:

$$\sigma_{xx}(H) = \frac{\rho_{xx}(H)}{\rho_{xx}^2(H) + \rho_{yx}^2(H)}, \quad (\text{S3})$$

$$\sigma_{xy}(H) = \frac{\rho_{yx}(H)}{\rho_{xx}^2(H) + \rho_{yx}^2(H)}. \quad (\text{S4})$$

To facilitate further analysis, we normalize $\sigma_{xx}(H)$ and $\sigma_{xy}(H)$ by the zero-field conductivity $\sigma_{xx}(0)$, defining the dimensionless magnetoconductivity $X(H)$ and Hall conductivity $Y(H)$

as follows:

$$X(H) = \frac{\sigma_{xx}(H)}{\sigma_{xx}(0)}, \quad (\text{S5})$$

$$Y(H) = \frac{\sigma_{xy}(H)}{\sigma_{xx}(0)}. \quad (\text{S6})$$

As discussed in the next subsection, these normalized quantities are essential for performing the Kramers-Kronig (KK) transformation to separate the electron and hole carrier contributions to the conductivity.

2. Electron-hole separation

To obtain the mobility spectrum from the magnetotransport data, it is essential to separate the contributions of electron and hole carriers. Due to the multi-band nature of the present system, the electron and hole contributions in $X(H)$ and $Y(H)$ partially cancel each other, leading to ambiguity in the analysis process. To overcome this issue, we employ a three-step procedure: (i) Lorentzian fitting, (ii) KK transformation, and (iii) carrier separation. Each step is described in detail below.

2.1 Lorentzian fitting

In general, $X(H)$ and $Y(H)$ can be expressed as a sum of Lorentzian functions with respect to the magnetic field. As will be discussed below, the KK transformation of $X(H)$ and $Y(H)$ requires knowledge of their values across the entire range of H . To achieve this, we fit the experimental data using a linear combination of Lorentzian functions, allowing us to determine their values in the high-field region. The fitting functions are given by

$$X(H) = \sum_{j=1}^n \frac{a_j}{1 + \mu_j^2 B^2}, \quad (\text{S7})$$

$$Y(H) = \sum_{j=1}^n \frac{b_j B}{1 + \mu_j^2 B^2}, \quad (\text{S8})$$

where n is the total number of Lorentzian functions, a_j , b_j , and μ_j are fitting parameters for the j -th Lorentzian function, and $B = \mu_0 H$ is the magnetic flux density.

In our initial analysis, we found that choosing $n = 4$ or 5 provided a reasonable fit to the experimental data. However, the exact value of n does not carry significant physical meaning.

The primary purpose of this fitting procedure is to ensure that $X(H)$ and $Y(H)$ have well-defined values over the entire magnetic field range, which is necessary for performing the KK transformation. The fitting results using the sum of the Lorentzian functions described above are shown in Figs. S3(a) and S3(b).

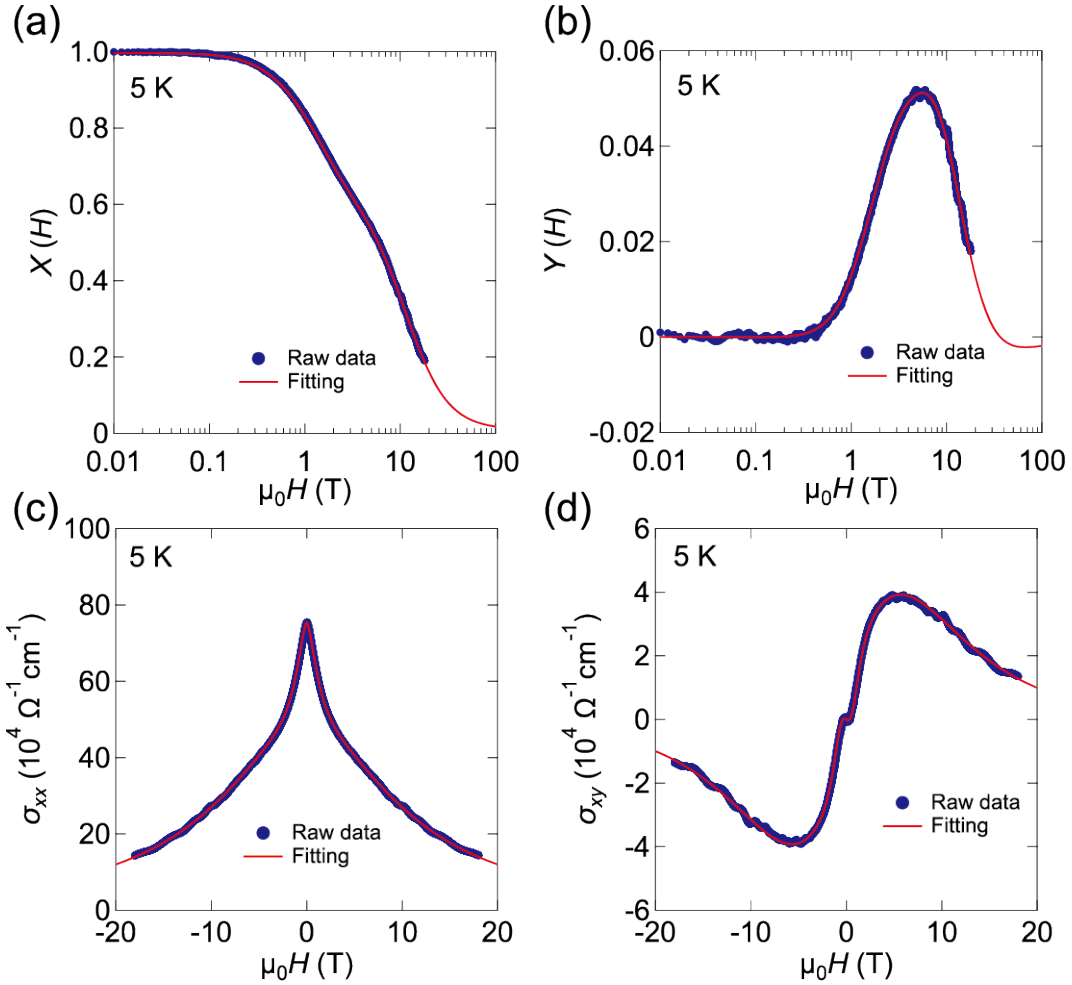


FIG. S3. (a), (b) $X(H)$ and $Y(H)$ at 5 K for pristine CsV_3Sb_5 , respectively. The red lines represent Lorentzian fits to the experimental results (blue). (c), (d) Comparison between experimental and fitting results for $\sigma_{xx}(H)$ and $\sigma_{xy}(H)$, respectively.

2.2 Kramers-Kronig (KK) transformation

To separate the contributions of electron and hole carriers, we apply the KK transformation to $X(H)$ and $Y(H)$ using the following expressions:

$$X'(H) = \mathcal{P} \frac{1}{\pi} \int_{-\infty}^{\infty} \frac{X(H')}{\mu_0 H - \mu_0 H'} dH' = Y^p(H) - Y^n(H), \quad (\text{S9})$$

$$Y'(H) = \mathcal{P} \frac{1}{\pi} \int_{-\infty}^{\infty} \frac{Y(H')}{\mu_0 H - \mu_0 H'} dH' = -X^p(H) + X^n(H), \quad (\text{S10})$$

where \mathcal{P} denotes the Cauchy principal value, and the superscripts p and n indicate contributions from hole and electron carriers, respectively. Equations (S9) and (S10) show that $X'(H)$ and $Y'(H)$ can be divided into the hole and electron carrier contributions. In practical calculations, the integration range is inevitably finite. Therefore, in this study, to perform the KK transformation accurately, we set the integration range from -10^6 T to 10^6 T so that $X(H)$ and $Y(H)$ approach zero within the integration range. This minimizes numerical artifacts and improves the accuracy of the KK transformation.

2.3 Carrier separation

In general, the following relations hold for $X(H)$ and $Y(H)$:

$$X(H) = X^p(H) + X^n(H), \quad (\text{S11})$$

$$Y(H) = Y^p(H) + Y^n(H). \quad (\text{S12})$$

Using these equations along with Eqs. (S9) and (S10), we obtain explicit expressions for $X^p(H)$, $X^n(H)$, $Y^p(H)$, and $Y^n(H)$ as follows:

$$X^p(H) = \frac{1}{2} [X(H) - Y'(H)], \quad (\text{S13})$$

$$X^n(H) = \frac{1}{2} [X(H) + Y'(H)], \quad (\text{S14})$$

$$Y^p(H) = \frac{1}{2} [Y(H) + X'(H)], \quad (\text{S15})$$

$$Y^n(H) = \frac{1}{2} [Y(H) - X'(H)]. \quad (\text{S16})$$

These relations allow us to separately evaluate the contributions of hole and electron carriers to the conductivity. The obtained results are presented in Figs. 3(a) and (b) in the main text.

3. μ -spectrum method

3.1 Decomposition of $X^{p,n}(H)$ and $Y^{p,n}(H)$

In the first step of the μ -spectrum method, we decompose $X^{p,n}(H)$ and $Y^{p,n}(H)$ into a sum of Lorentzian functions. In general, as discussed in the main text, $X^{p,n}(H)$ and $Y^{p,n}(H)$ can be expressed as an integral of Lorentzian functions with respect to the carrier mobility μ (see Eqs. (1) and (2) in the main text). If $s^{p,n}(\mu)$ can be determined as a function of μ , the conductivity-mobility spectrum can be obtained. To achieve this, we discretize the integral expression by introducing a small interval $\Delta\mu$. However, choosing $\Delta\mu$ with an equal spacing would lead to a large ambiguity in the low-field region. Instead, we define the discretization such that $\ln(\mu)$ is evenly spaced, i.e., we set the interval as $\Delta m = \Delta \ln(\mu)$. Using this formulation, $X^{p,n}(H)$ and $Y^{p,n}(H)$ are expressed as a sum of Lorentzian functions as follows:

$$X^{p,n}(H) = \sum_{j=1}^N \frac{\exp(m_j) s^{p,n}(m_j) \Delta m}{1 + \exp[2(m_j + b)]}, \quad (\text{S17})$$

$$Y^{p,n}(H) = \sum_{j=1}^N \frac{\exp(m_j) s^{p,n}(m_j) \Delta m}{2 \cosh(m_j + b)}, \quad (\text{S18})$$

where $m = \ln(\mu)$, $b = \ln(B)$, N represents the number of divisions used for discretization, and $s^{p,n}(\mu)$ is the conductivity-mobility spectrum. Here, m is divided into $N = 1000$ segments, ranging from -6 to 4 with an interval of $\Delta m = 0.01$. Similarly, b is also discretized into 1000 points, ranging from -6 to 4 with an interval of $\Delta b = 0.01$. This discretization allows $X^{p,n}(H)$ and $Y^{p,n}(H)$ to be expressed in matrix form as follows:

$$\begin{pmatrix} X^{p,n}(b_1) \\ X^{p,n}(b_2) \\ \vdots \\ X^{p,n}(b_N) \end{pmatrix} = \begin{pmatrix} \frac{\exp(m_1)\Delta m}{1+\exp[2(m_1+b_1)]} & \cdots & \frac{\exp(m_N)\Delta m}{1+\exp[2(m_N+b_1)]} \\ \frac{\exp(m_1)\Delta m}{1+\exp[2(m_1+b_2)]} & \cdots & \frac{\exp(m_N)\Delta m}{1+\exp[2(m_N+b_2)]} \\ \vdots & \ddots & \vdots \\ \frac{\exp(m_1)\Delta m}{1+\exp[2(m_1+b_N)]} & \cdots & \frac{\exp(m_N)\Delta m}{1+\exp[2(m_N+b_N)]} \end{pmatrix} \begin{pmatrix} s^{p,n}(m_1) \\ s^{p,n}(m_2) \\ \vdots \\ s^{p,n}(m_N) \end{pmatrix}, \quad (\text{S19})$$

$$\begin{pmatrix} Y^{p,n}(b_1) \\ Y^{p,n}(b_2) \\ \vdots \\ Y^{p,n}(b_N) \end{pmatrix} = \begin{pmatrix} \frac{\exp(m_1)\Delta m}{2\cosh(m_1+b_1)} & \cdots & \frac{\exp(m_N)\Delta m}{2\cosh(m_N+b_1)} \\ \frac{\exp(m_1)\Delta m}{2\cosh(m_1+b_2)} & \cdots & \frac{\exp(m_N)\Delta m}{2\cosh(m_N+b_2)} \\ \vdots & \ddots & \vdots \\ \frac{\exp(m_1)\Delta m}{2\cosh(m_1+b_N)} & \cdots & \frac{\exp(m_N)\Delta m}{2\cosh(m_N+b_N)} \end{pmatrix} \begin{pmatrix} s^{p,n}(m_1) \\ s^{p,n}(m_2) \\ \vdots \\ s^{p,n}(m_N) \end{pmatrix}. \quad (\text{S20})$$

3.2 Solving for $s^{p,n}$

In the second step of the μ -spectrum method, we determine $s^{p,n}(m_j)$ for each m_j through Eqs. (S19) and (S20) obtained in the previous step. To achieve this, we substitute numerical values for b_j and m_j within the range of -6 to 4 and solve the matrix equations to obtain $s^{p,n}(m_j)$. In general, to obtain a set of $s^{p,n}(m_j)$, it is necessary to compute the inverse of an $N \times N$ matrix. However, the inverse matrix for large N generally involves uncertainty. Then, in this study, we search for $s^{p,n}$ that minimizes the difference between the left-hand and right-hand sides of Eqs. (S19) and (S20). To this end, first, we set all initial parameters of $s^{p,n}(m_j)$ to zero and optimized $s^{p,n}(m_j)$ for $X^{p,n}(H)$. The optimized values are then used as the initial parameters for $Y^{p,n}(H)$. This process is repeated, alternating between $X^{p,n}(H)$ and $Y^{p,n}(H)$, until the obtained $s^{p,n}(m_j)$ converged to consistent values, because $X^{p,n}(H)$ and $Y^{p,n}(H)$ should be described by the same set of $s^{p,n}(m_j)$. For computational efficiency, we utilized a GPU-based fitting package [S5]. The obtained conductivity-mobility spectrum is presented in Figs. 3(c) and 3(d) in the main text.

3.3 Calculation of μ_i and S_i

In the final step of the μ -spectrum method, we calculate the averaged mobility for each carrier and the contribution of each carrier to the total conductivity. The obtained mobility spectrum exhibits three characteristic peak structures for both electron and hole carriers (see Figs. 3(c) and 3(d) in the main text). To determine the mobility and conductivity associated with each carrier, it is crucial to define these quantities properly, given the broad nature of the peaks. To address this, we define the averaged mobility (μ_i) and the contribution of each peak i ($= h_1-h_3, e_1-e_3$) to the total conductivity (S_i) using the following expressions:

$$\mu_i = \frac{\sum_{\mu-\epsilon}^{\mu+\epsilon} \mu s(\mu) \Delta\mu}{\sum_{\mu-\epsilon}^{\mu+\epsilon} s(\mu) \Delta\mu}, \quad (\text{S21})$$

$$S_i = \sum_{\mu-\epsilon}^{\mu+\epsilon} s(\mu) \Delta\mu, \quad (\text{S22})$$

where the summations are taken over each peak i with the peak width of 2ϵ . The extracted results are presented in Figs. 3(g) and 3(h) in the main text. Through the μ -spectrum method, we obtained the following relationship between the averaged mobility μ_i and the

carrier density n_i for each carrier using S_i :

$$\sigma_{xx}(0)S_i = n_i e \mu_i. \quad (\text{S23})$$

4. 2DMAT fitting

To obtain more accurate mobility and carrier density, we fit $\sigma_{xx}(H)$ and $\sigma_{xy}(H)$ simultaneously using the values obtained from the μ -spectrum method as initial parameters. This procedure allows us to refine the mobility and carrier density for each carrier (see Figs. S3(c) and S3(d)). We applied the 2DMAT program [S6] to simultaneously fit both σ_{xx} and σ_{xy} . The expressions used for fitting σ_{xx} and σ_{xy} are given by:

$$\sigma_{xx}(H) = \sum_{j=1}^3 \frac{n_{h_j} e \mu_{h_j}}{1 + \mu_{h_j}^2 B^2} - \sum_{j=1}^3 \frac{n_{e_j} e \mu_{e_j}}{1 + \mu_{e_j}^2 B^2}, \quad (\text{S24})$$

$$\sigma_{xy}(H) = \sum_{j=1}^3 \frac{n_{h_j} e \mu_{h_j}^2 B}{1 + \mu_{h_j}^2 B^2} - \sum_{j=1}^3 \frac{n_{e_j} e \mu_{e_j}^2 B}{1 + \mu_{e_j}^2 B^2}. \quad (\text{S25})$$

The optimized parameters obtained from 2DMAT fitting are then used as new initial values to restart the iterative process from the Lorentzian fitting in step 2 (see Fig. S2). The entire sequence of calculations is repeated until the extracted mobility and carrier density converged. Once convergence is achieved, the final mobility and carrier density are determined, completing the analysis.

III. QUANTUM OSCILLATION ANALYSIS

Quantum oscillations offer valuable insights into the electronic structure of materials. By analyzing the oscillatory components of transport measurements in a magnetic field, we can extract key parameters such as the Fermi surface topology, effective mass, and carrier scattering rates. In this section, we present the quantum oscillation analysis conducted on the 3 C/cm^2 irradiated sample. Figure S4(a) shows the quantum oscillation components of the magnetoresistance for the 3 C/cm^2 irradiated CsV_3Sb_5 sample. Figure S4(b) presents the fast Fourier transform (FFT) of the oscillatory components, revealing peaks at approximately 20 T, 70 T, and 90 T, which are labeled as α/β , γ , and δ , respectively. Figure S4(c) displays the temperature dependence of the FFT amplitude for each orbit, from which the effective mass can be extracted. Notably, electron irradiation almost does not alter the frequency and effective mass of each orbit, indicating that the electronic structure remains unaffected by electron irradiation. Instead, only the carrier scattering rate is changed. Figure S4(d) presents the Landau fan diagram for both the pristine and 3 C/cm^2 irradiated samples. As reported in previous studies, the α and γ orbits exhibit a nontrivial Berry phase, whereas the Berry phases of the β and δ orbits are nearly zero. This result suggests that the α and γ orbits may be associated with Dirac bands. It should be noted that even if a nontrivial band topology with a finite Berry curvature is present, its contribution to the Hall conductivity is at most about $1,000\ \Omega^{-1}\text{cm}^{-1}$, as discussed in other anomalous Hall systems [S7–S15] (see Fig. S6). Therefore, it is unlikely that the non-monotonic Hall effect observed in CsV_3Sb_5 comes from the non-trivial band topology. Furthermore, electron irradiation of 3 C/cm^2 does not change the Berry phase of the γ orbit, while the non-monotonic Hall effect is no longer observed after electron irradiation. This also confirms that the nontrivial band topology is not related to the hole anomaly observed in CsV_3Sb_5 .

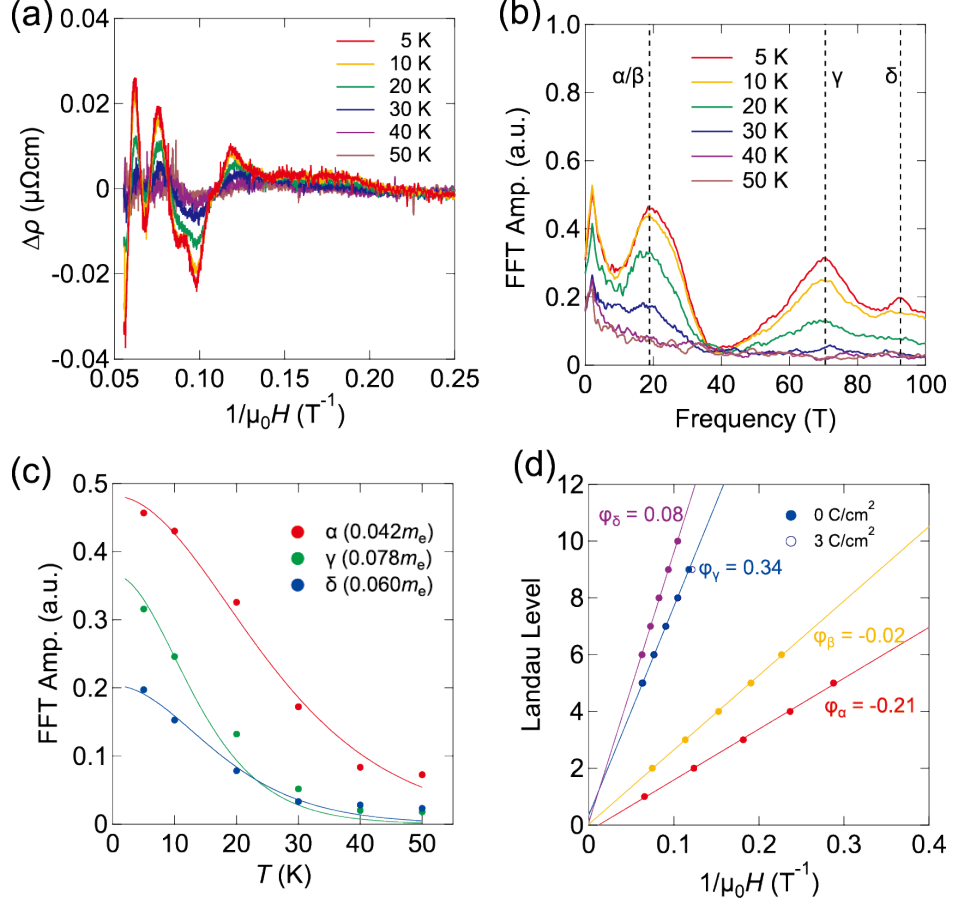


FIG. S4. (a) Oscillatory components extracted from the magnetoresistivity for the 3 C/cm^2 irradiated sample at various temperatures. (b) FFT spectrum of the 3 C/cm^2 irradiated sample at various temperatures. Three peaks (α/β , γ , and δ orbits) are observed, in addition to the first peak at the lowest frequency ($\sim 3 \text{ T}$), which is an artifact of the FFT. (c) Temperature dependence of FFT amplitude for each peak. The solid lines represent the Lifshitz-Kosevich formula. (d) Landau fan diagram plot of the pristine and 3 C/cm^2 irradiated CsV_3Sb_5 samples.

IV. COMPARISON BETWEEN QUANTUM OSCILLATION EXPERIMENTS AND μ -SPECTRUM ANALYSIS

We compare the results of quantum oscillation measurements and μ -spectrum analysis. Table S1 summarizes the correspondence between the carriers identified by these two methods. The peaks h_2, h_3, e_2 , and e_3 identified in the μ -spectrum analysis exhibit low carrier densities, which are likely related to the low-frequency orbits α, β, γ , and δ detected in the quantum oscillations. These results suggest that they originate from small Fermi pockets below the CDW transition. The carrier densities estimated from the two methods differ by a factor of several. This discrepancy may arise because quantum oscillation measurements provide the carrier density for a single orbit, whereas in μ -spectrum analysis, the estimated carrier density includes contributions from multiple identical Fermi surfaces within the BZ. The peaks h_1 and e_1 are considered to correspond to the high-frequency branches μ and ν reported in a previous quantum oscillation study [S16], which are associated with the Fermi surfaces around the Γ and K points in the original BZ. Band structure calculations indicate that these Fermi surfaces persist without significant reconstruction across the CDW transition. The observation of peaks h_1 and e_1 in the μ -spectrum analysis above the CDW transition supports the validity of our present arguments.

TABLE S1. Comparisons between the quantum oscillation experiments and μ -spectrum analysis. The frequency F and carrier density n of each branch observed in the quantum oscillation experiments are listed, where n corresponds to a single Fermi surface orbit. The peaks and corresponding carrier densities obtained from the μ -spectrum analysis are also listed.

Quantum oscillations			μ -spectrum analysis	
Branch	F (T)	n (cm $^{-3}$)	Peak	n (cm $^{-3}$)
α	18	9.35×10^{18}	h_3	$(2.58 \pm 1.25) \times 10^{18}$
β	25	1.30×10^{19}	e_3	$(4.26 \pm 0.31) \times 10^{19}$
γ	73	3.79×10^{19}	h_2	$(1.29 \pm 0.47) \times 10^{20}$
δ	93	4.83×10^{19}	e_2	$(0.84 \pm 0.36) \times 10^{20}$
μ [S16]	1700	8.83×10^{20}	h_1	$(1.64 \pm 0.52) \times 10^{21}$
ν [S16]	1930	1.00×10^{21}	e_1	$(1.75 \pm 0.48) \times 10^{21}$

V. NON-MONOTONIC COMPONENTS OF HALL EFFECT

To extract the non-monotonic component of the Hall resistivity $\rho_{yx}^{\text{NM}}(H)$, we used the following formula:

$$\rho_{yx}^{\text{NM}}(H) = \rho_{yx}(H) - cH, \quad (\text{S26})$$

where c is the coefficient extracted from a linear fit of $\rho_{yx}(H)$ over the magnetic field range of 0–2 T. $\rho_{yx}^{\text{NM}}(H)$ was then converted into the non-monotonic Hall conductivity $\sigma_{xy}^{\text{NM}}(H)$ using the following equation:

$$\sigma_{xy}^{\text{NM}}(H) = \frac{\rho_{yx}^{\text{NM}}(H)}{\rho_{xx}^2(H) + \rho_{yx}^2(H)}. \quad (\text{S27})$$

The obtained results for the pristine, 3 C/cm², and 8.6 C/cm²-irradiated samples are presented in Fig. S5.

Here, we compare the obtained non-monotonic Hall conductivity with other materials exhibiting anomalous Hall effects [S7–S15] (see Fig. S6). Notably, the non-monotonic component of the Hall conductivity in CsV₃Sb₅ is an order of magnitude larger than those of other materials that exhibit intrinsic anomalous Hall effects. Moreover, we have observed that σ_{xy}^{NM} is proportional to σ_{xx}^2 , which is distinctly different from behaviors observed in other anomalous Hall systems. In CsV₃Sb₅, the low-field Hall resistivity is much smaller than the magnetoresistivity, allowing the magnetoconductivity and Hall conductivity to be approximated as:

$$\sigma_{xx}(H) = \frac{\rho_{xx}(H)}{\rho_{xx}^2(H) + \rho_{yx}^2(H)} \approx \frac{1}{\rho_{xx}(H)}, \quad (\text{S28})$$

$$\sigma_{xy}(H) = \frac{\rho_{yx}(H)}{\rho_{xx}^2(H) + \rho_{yx}^2(H)} \approx \frac{\rho_{yx}(H)}{\rho_{xx}^2(H)} \approx \rho_{yx}(H)\sigma_{xx}^2(H). \quad (\text{S29})$$

These relations lead to $\sigma_{xy} \propto \sigma_{xx}^2$, indicating that the non-monotonic component of the Hall conductivity is attributed to the conventional Drude mechanism such as skew scattering. Furthermore, our μ -spectrum analysis has revealed the presence of extremely high-mobility carriers associated with small Fermi pockets. Considering these findings, we conclude that the non-monotonic Hall effect in CsV₃Sb₅ does not arise from an anomalous Hall effect but rather originates from high-mobility carriers in small Fermi pockets. Our present findings highlight the importance of high-mobility carriers in the Hall response of CsV₃Sb₅.

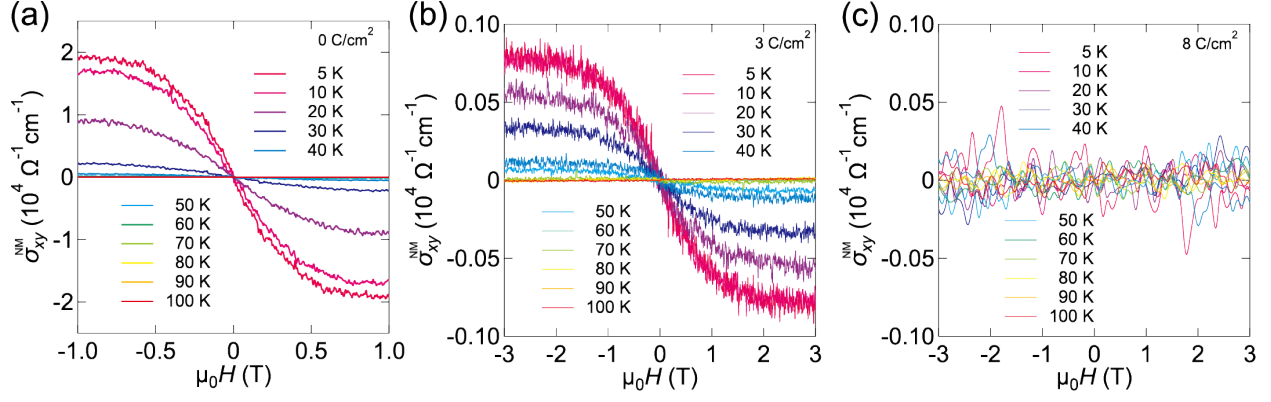


FIG. S5. (a)-(c) Non-monotonic components of the Hall conductivity for (a) pristine, (b) 3 C/cm², and (c) 8.6 C/cm² irradiated CsV₃Sb₅ samples.

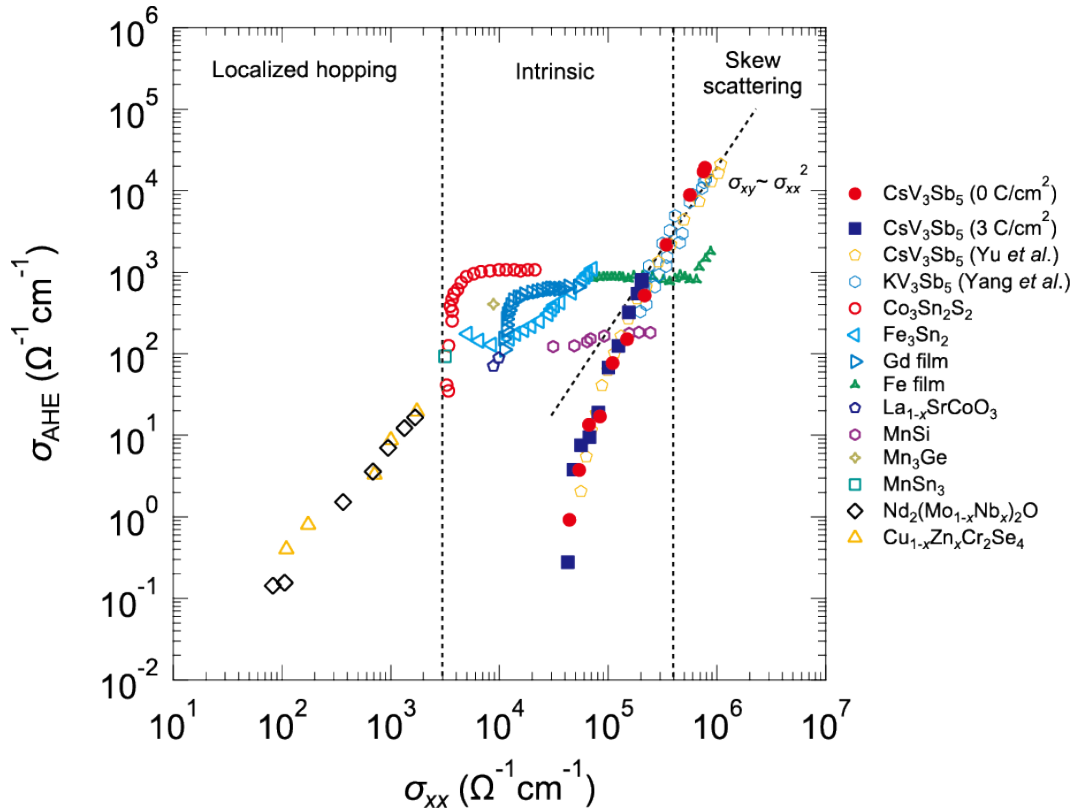


FIG. S6. σ_{AHE} vs. σ_{xx} for a variety of materials. σ_{xy}^{NM} vs. σ_{xx} for CsV₃Sb₅ and KV₃Sb₅, including our present results as well as those from previous studies [S17, S18], is also plotted. The quadratic scaling between σ_{AHE} and σ_{xx} is shown as the dashed line.

Supplementary References

- [S1] J. W. McClure, Analysis of multicarrier galvanomagnetic data for graphite, *Phys. Rev.* **112**, 715 (1958).
- [S2] W. A. Beck and J. R. Anderson, Determination of electrical transport properties using a novel magnetic field-dependent Hall technique, *Journal of Applied Physics* **62**, 541 (1987).
- [S3] J. Antoszewski, G. A. Umana-Membreno, and L. Faraone, High-resolution mobility spectrum analysis of multicarrier transport in advanced infrared materials, *Journal of Electronic Materials* **41**, 2816 (2012).
- [S4] K. K. Huynh, Y. Tanabe, T. Urata, S. Heguri, K. Tanigaki, T. Kida, and M. Hagiwara, Mobility spectrum analytical approach for intrinsic band picture of Ba(FeAs)₂, *New Journal of Physics* **16**, 093062 (2014).
- [S5] A. Przybylski, B. Thiel, J. Keller-Findeisen, B. Stock, and M. Bates, Gpufit: An open-source toolkit for GPU-accelerated curve fitting, *Scientific Reports* **7**, 15722 (2017).
- [S6] Y. Motoyama, K. Yoshimi, I. Mochizuki, H. Iwamoto, H. Ichinose, and T. Hoshi, Data-analysis software framework 2DMAT and its application to experimental measurements for two-dimensional material structures, *Computer Physics Communications* **280**, 108465 (2022).
- [S7] T. Miyasato, N. Abe, T. Fujii, A. Asamitsu, S. Onoda, Y. Onose, N. Nagaosa, and Y. Tokura, Crossover behavior of the anomalous Hall effect and anomalous Nernst effect in itinerant ferromagnets, *Phys. Rev. Lett.* **99**, 086602 (2007).
- [S8] S. Iguchi, N. Hanasaki, and Y. Tokura, Scaling of anomalous Hall resistivity in Nd₂(Mo_{1-x}Nb_x)₂O₇ with spin chirality, *Phys. Rev. Lett.* **99**, 077202 (2007).
- [S9] N. Kanazawa, Y. Onose, T. Arima, D. Okuyama, K. Ohoyama, S. Wakimoto, K. Kakurai, S. Ishiwata, and Y. Tokura, Large topological Hall effect in a short-period helimagnet MnGe, *Phys. Rev. Lett.* **106**, 156603 (2011).
- [S10] S. Nakatsuji, N. Kiyohara, and T. Higo, Large anomalous Hall effect in a non-collinear antiferromagnet at room temperature, *Nature* **527**, 212 (2015).
- [S11] A. K. Nayak, J. E. Fischer, Y. Sun, B. Yan, J. Karel, A. C. Komarek, C. Shekhar, N. Kumar,

- W. Schnelle, J. Kübler, C. Felser, and S. S. P. Parkin, Large anomalous Hall effect driven by a nonvanishing Berry curvature in the noncolinear antiferromagnet Mn_3Ge , *Science Advances* **2**, e1501870 (2016).
- [S12] L. Ye, M. Kang, J. Liu, F. von Cube, C. R. Wicker, T. Suzuki, C. Jozwiak, A. Bostwick, E. Rotenberg, D. C. Bell, L. Fu, R. Comin, and J. G. Checkelsky, Massive Dirac fermions in a ferromagnetic kagome metal, *Nature* **555**, 638 (2018).
- [S13] E. Liu, Y. Sun, N. Kumar, L. Muechler, A. Sun, L. Jiao, S.-Y. Yang, D. Liu, A. Liang, Q. Xu, J. Kroder, V. S. H. Borrmann, C. Shekhar, Z. Wang, C. Xi, W. Wang, W. Schnelle, S. Wirth, Y. Chen, S. T. B. Goennenwein, and C. Felser, Giant anomalous Hall effect in a ferromagnetic kagome lattice semimetal, *Nature Physics* **14**, 1125 (2018).
- [S14] T. Kurumaji, T. Nakajima, M. Hirschberger, A. Kikkawa, Y. Yamasaki, H. Sagayama, H. Nakao, Y. Taguchi, T. Arima, and Y. Tokura, Skyrmion lattice with a giant topological hall effect in a frustrated triangular-lattice magnet, *Science* **365**, 914 (2019).
- [S15] Y. Fujishiro, N. Kanazawa, R. Kurihara, H. Ishizuka, T. Hori, F. S. Yasin, X. Yu, A. Tsukazaki, M. Ichikawa, M. Kawasaki, N. Nagaosa, M. Tokunaga, and Y. Tokura, Giant anomalous Hall effect from spin-chirality scattering in a chiral magnet, *Nature Communications* **12**, 317 (2021).
- [S16] B. R. Ortiz, S. M. L. Teicher, L. Kautzsch, P. M. Sarte, N. Ratcliff, J. Harter, J. P. C. Ruff, R. Seshadri, and S. D. Wilson, Fermi surface mapping and the nature of charge-density-wave order in the kagome superconductor CsV_3Sb_5 , *Phys. Rev. X* **11**, 041030 (2021).
- [S17] F. H. Yu, T. Wu, Z. Y. Wang, B. Lei, W. Z. Zhuo, J. J. Ying, and X. H. Chen, Concurrence of anomalous Hall effect and charge density wave in a superconducting topological kagome metal, *Phys. Rev. B* **104**, L041103 (2021).
- [S18] S.-Y. Yang, Y. Wang, B. R. Ortiz, D. Liu, J. Gayles, E. Derunova, R. Gonzalez-Hernandez, L. Šmejkal, Y. Chen, S. S. P. Parkin, S. D. Wilson, E. S. Toberer, T. McQueen, and M. N. Ali, Giant, unconventional anomalous Hall effect in the metallic frustrated magnet candidate, KV_3Sb_5 , *Science Advances* **6**, eabb6003 (2020).